Catheterization and Cardiovascular Interventions

WILEY

ORIGINAL ARTICLE - CLINICAL SCIENCE OPEN ACCESS

Preclinical Serial Assessment of Virtual Physiology After Implantation of a Novel Endoluminal Resorbable Fibrillated Scaffold

Kotaro Miyashita[1,2] | Lucas Hatzikostas[3,4] | Emiliano Bianchini[1] | Milosz Dziarmaga[5] | Chun-Ting Shih[1,6] | Jouke Dijkstra[7] | Eric K. W. Poon[3] | Bart Sanders[8] | Golo von Basum[8] | Rick de Vries[8] | Kim van Noort[8] | Marc van Sambeek[9] | Jos C. van den Berg[10] | Albert Chinhenzva[1] | Scot Garg[11,12] | Yoshinobu Onuma[1] | Patrick W. Serruys[1]

[1]CORRIB Research Centre for Advanced Imaging and Core Lab, University of Galway, Galway, Ireland | [2]Department of Cardiology, Ageo Central General Hospital, Saitama, Japan | [3]Department of Medicine, Melbourne Medical School, Faculty of Medicine, Dentistry and Health Sciences, The University of Melbourne, Fitzroy, Victoria, Australia | [4]Department of Cardiology, Royal Melbourne Hospital, Parkville, Victoria, Australia | [5]Department of Cardiology, Intensive Therapy and Internal Medicine, Poznan University of Medical Sciences, Poznan, Poland | [6]Department of Internal Medicine, Division of Cardiology, Kaohsiung Chang Gung Memorial Hospital, Kaohsiung, Taiwan | [7]Department of Radiology, Division of Image Processing, Leiden University Medical Center, Leiden, the Netherlands | [8]Stentit B.V., Eindhoven, the Netherlands | [9]Department of Vascular Surgery, Catharina Hospital, Eindhoven, the Netherlands | [10]Clinica Luganese Moncucco, Lugano, Switzerland | [11]Department of Cardiology, Royal Blackburn Hospital, Blackburn, UK | [12]School of Medicine, University of Central Lancashire, Preston, UK

Correspondence: Patrick W. Serruys (patrick.w.j.c.serruys@gmail.com)

Received: 24 January 2026 | **Revised:** 9 June 2026 | **Accepted:** 9 July 2026

Funding: STENTiT B.V.

Keywords: bioresorbable scaffold | optical coherence tomography | peripheral artery disease | quantitative flow ratio | resorbable fibrillated scaffold | virtual physiology

ABSTRACT

Background: The resorbable fibrillated scaffold (RFS) is a novel electrospun, polylactide-based endoluminal scaffold developed for peripheral arterial applications. Its porous microfibre architecture is intended to support host cell infiltration and vascular restoration. Although its near-wall hemodynamic behaviour has been characterised, its serial anatomical and virtual physiological evolution after implantation has not previously been examined.

Aims: To characterise the serial anatomical changes of the RFS after implantation in peripheral arterial models, and to assess the hemodynamic significance of luminal narrowing during follow-up using image-derived virtual flow indices.

Methods: Two preclinical studies were conducted in rabbit and mini-pig peripheral arterial models. The RFS was implanted bilaterally in the external iliac arteries of three rabbits and in the profunda femoris arteries of six mini-pigs. Serial follow-up to 3 months was performed using invasive angiography and intravascular optical coherence tomography (OCT) for anatomical assessment. Virtual physiology was assessed using angiography-derived Murray-law-based quantitative flow ratio (μFR) and OCT-derived flow ratio (OFR).

Results: Implantation was technically successful in all but one case. In rabbits, between post-implantation and 3 months, reference vessel diameter increased from 2.08 to 2.54 mm ($p = 0.03$), while minimum lumen diameter remained stable; OCT-derived area stenosis increased from 28.9% to 56.1% ($p < 0.01$), scaffold length shortened from 10.40 to 8.63 mm ($p < 0.01$),

Abbreviations: AS, area stenosis; BTK, below-the-knee; DS, diameter stenosis; FFR, fractional flow reserve; MLA, minimum lumen area; MLD, minimum lumen diameter; OCT, optical coherence tomography; OFR, OCT-derived flow ratio; RFS, resorbable fibrillated scaffold; μFR, angiography-derived Murray-law-based quantitative flow ratio.

Kotaro Miyashita and Lucas Hatzikostas contributed equally to this work and share co-first authorship.

and μFR decreased from 0.99 to 0.92 ($p = 0.04$), whereas OFR remained unchanged. In mini-pigs, the principal changes occurred between post-implantation and 1 month, with reductions in minimum lumen diameter, minimum lumen area, μFR, and OFR (all $p \leq 0.03$), accompanied by increased stenosis and relative stabilization thereafter. Both μFR and OFR declined non-linearly with increasing OCT-derived %AS, with similar model fit ($R^2 = 0.57$).

Conclusion: This preclinical study supports the feasibility of RFS implantation in peripheral arteries and demonstrates that the device undergoes early structural evolution after deployment. Virtual physiological assessment showed that these anatomical changes were accompanied by measurable reductions in flow indices, though most values remained above the 0.80 reference threshold. Together, these findings provide a basis for further development of the technology and for future studies incorporating both anatomical and virtual physiological assessment.

1 | Introduction

Peripheral artery disease affects more than 110 million people worldwide and is associated with major adverse limb events, amputation, and excess cardiovascular mortality [1]. In infrapopliteal, or below-the-knee (BTK), disease, plain balloon angioplasty remains the principal endovascular treatment, while stenting is generally reserved for bail-out use in the setting of recoil, dissection, or other suboptimal angioplasty results [2]. Although metallic drug-eluting stents can reduce restenosis in selected short lesions, their permanent endoluminal cage may impair normal vessel biology [3], limit adaptive remodeling, and complicate future surgical or endovascular reintervention [4, 5]. These limitations have sustained interest in bioresorbable scaffold technologies designed to provide temporary mechanical support and then gradually disappear once vascular healing is established [6].

Early poly-L-lactic acid scaffold platforms demonstrated proof of concept, but broader adoption was limited by thick struts, slow and heterogeneous degradation, and an increased risk of late scaffold-related events [7]. Newer bioresorbable platforms are therefore being developed to improve deliverability, healing, and longer-term vascular restoration [8, 9]. Resorbable strategies are also being explored in peripheral arterial disease, including BTK revascularisation [10, 11].

The resorbable fibrillated scaffold (RFS) (STENTiT B.V., Eindhoven, the Netherlands) is a novel electrospun endoluminal scaffold composed of polylactide-based co-polymers. Unlike conventional strut-based scaffold designs, it is tubular and consists of a highly porous fibrillated microfibre matrix intended to provide temporary luminal support while permitting cellular infiltration and tissue integration [12]. The device was developed for peripheral arterial applications and has now entered early clinical evaluation in BTK disease (VITAL-IT 1; NCT07006467).

A recent study described, for the first time, the intravascular optical coherence tomography (OCT) appearance of the RFS and examined its multidirectional wall shear stress profile in two preclinical models [13]. However, although the near-wall hemodynamic behavior of the scaffold has been characterized, its serial anatomical and virtual physiological evolution has not previously been examined.

The present study addresses this question in a partially overlapping preclinical serial imaging cohort. Specifically, we evaluated image-derived virtual flow indices, including angiography-derived Murray-law-based quantitative flow ratio (μFR) and OCT-derived flow ratio (OFR), to assess the hemodynamic significance of luminal narrowing during follow-up after RFS implantation.

2 | Methods

2.1 | Study Design and Animal Models

Two preclinical studies were conducted to evaluate the RFS in rabbit and mini-pig models. All animal experiments were approved by the institutional ethical committee on animal care and experimentation at Utrecht University and by the Central Authority for Scientific Procedures on Animals of the Netherlands. Project license numbers were AVD2290020186144 for the rabbit study and AVD22900202216226 for the porcine study. An overview of the study design is provided in Figure 1.

The rabbit study included three New Zealand White rabbits (Charles River, France), aged 12–15 weeks and weighing 2.4–2.8 kg. Animals underwent serial imaging follow-up over 3 months, with angiography performed pre-implantation, post-implantation, and at 3 months, and OCT acquired post-implantation and at 3-month follow-up. All rabbits were euthanized after completion of follow-up.

The mini-pig study included six Göttingen mini-pigs (Ellegaard, Dalmose, Denmark), aged 15–17 months and weighing 35.0–41.0 kg at implantation. Angiography and OCT were performed pre-implantation, post-implantation, and at 1- and 3-month follow-up. All mini-pigs were euthanized after the 3-month follow-up.

2.2 | Scaffold Implantation Procedure

Scaffold implantation was performed bilaterally in the intended target vessels in each model via carotid access. In rabbits, 2.0×10 mm RFS devices were implanted in the external iliac arteries, for a total of six scaffold implantations. In mini-pigs, 3.0×27 mm RFS devices were implanted in the profunda femoris arteries, for a total of 12 scaffold implantations. Because only off-the-shelf scaffold sizes were available, implantation sites were selected based on reference vessel diameter to achieve an approximately 1:1 match with the nominal scaffold inner diameter. Owing to scaffold thickness, this corresponded to approximately 10% oversizing relative to the scaffold outer

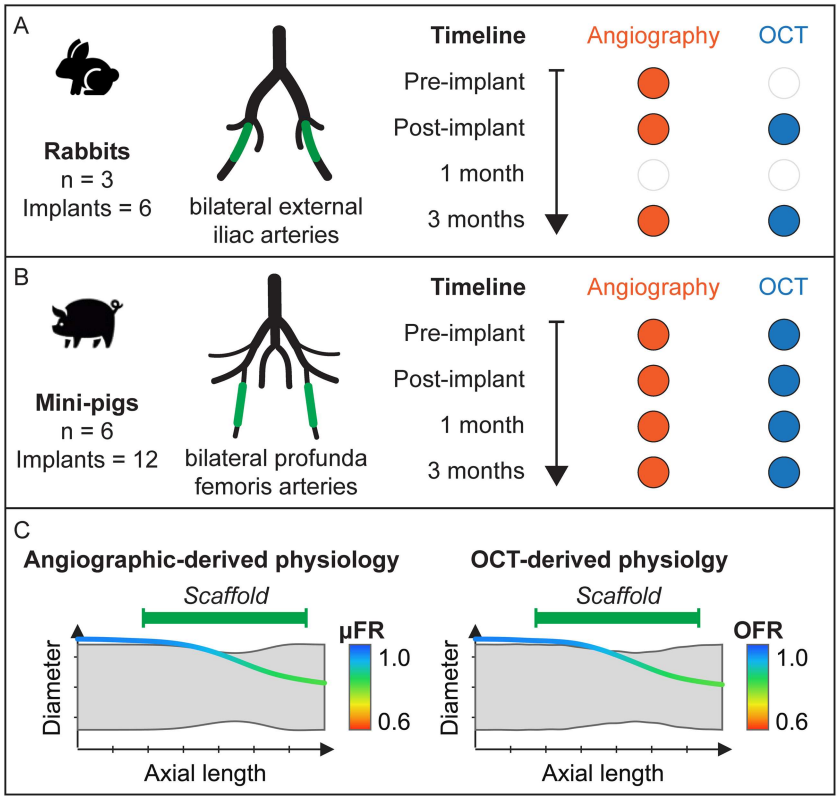

FIGURE 1 | Overview of the preclinical study design and representative virtual physiology assessment in rabbit and mini-pig models. (A, B) Schematic overview of the rabbit and mini-pig study cohorts, including the animal models, number of implanted scaffolds, target vessels, and serial imaging schedule. Target scaffold segments are highlighted in green and correspond to the bilateral external iliac arteries in rabbits and bilateral profunda femoris arteries in mini-pigs. Orange circles indicate invasive angiography, blue circles indicate intravascular OCT, and open circles indicate imaging time points that were not performed. (C) Representative virtual physiology profiles derived from angiographic geometry (μFR) and OCT geometry (OFR). Gray vessel contours represent modality-specific lumen geometry, the scaffolded segment is shown in green, and the colored pullback curves illustrate conceptual pressure-derived physiological profiles along the vessel axis. [Color figure can be viewed at wileyonlinelibrary.com]

diameter. Scaffolds were deployed using the nominal balloon expansion protocol without adjunctive post-dilatation. Technical success was defined as successful delivery and deployment of the scaffold in the intended target vessel segment, preservation of vessel patency at the end of the procedure, and absence of a major complication preventing procedural completion.

2.3 | Peri-Procedural Care and Antithrombotic Regimen

Rabbits and mini-pigs were housed and cared for at the gemeenschappelijk dierenlaboratorium (GDL) of Utrecht University under institutionally approved conditions. Rabbits were housed individually, whereas mini-pigs were group-housed, with environmental enrichment and welfare monitored throughout the study period. Species-specific anesthesia and analgesia protocols were used consistently during implantation and follow-up imaging sessions. Anesthetic depth was monitored throughout each procedure using standard physiological parameters, including heart rate, blood pressure, capnography, temperature, and reflex assessment, as appropriate to the animal model.

Antithrombotic therapy was maintained throughout the study period in both models. In rabbits, dual antiplatelet therapy was continued throughout follow-up, with procedural heparin administered and repeated as required. In mini-pigs, dual antiplatelet therapy was initiated before implantation and maintained throughout follow-up. After one early carotid access-site hematoma associated with the initial intra-procedural heparin regimen, the heparin dosing protocol was revised for subsequent procedures. Detailed species-specific dosing schedules are provided in the Supporting Information S1: Figures S1–S3.

2.4 | Angiographic Acquisition and Analysis

Invasive contrast angiography was acquired with the animal in the supine position using a single anteroposterior projection. Angiographic cine runs were exported in DICOM format and analyzed offline by the independent CORRIB Core Laboratory (University of Galway, Galway, Ireland) using AngioPlus software (Pulse Medical, Shanghai, China). To permit serial assessment of geometry over time, the same scaffolded vascular segment was identified at each imaging time point using fiducial landmarks, including side branches, for co-registration. Within the region of interest, conventional angiographic morphological measurements were obtained, including reference vessel diameter (RD), minimum lumen diameter (MLD), and percent diameter stenosis (%DS). In addition, angiography-derived

Murray-law-based quantitative flow ratio (μFR; Pulse Medical Imaging Technology, Shanghai, China), a surrogate of invasive pressure-wire physiology, was calculated. μFR was derived from the same angiographic projection, and assessed between identical proximal and distal landmarks during serial follow-up [14].

2.5 | OCT Acquisition and Analysis

Intravascular OCT was performed using a St. Jude Medical imaging system (St. Jude Medical, St. Paul, MN, USA) with an automatic pullback speed of 18 mm/s. OCT pullbacks were analyzed offline at the same core laboratory at 100 μm slice intervals. To enable comparison with angiography and serial assessment over follow-up, proximal and distal side branches visible on both modalities were used as anatomical landmarks. Conventional OCT-derived morphological measurements included reference vessel area (RA), minimum lumen area (MLA), percent area stenosis (%AS), and scaffold length (SL). The peri-scaffold segment was defined as the 5 mm proximal and 5 mm distal to the scaffold edges, and RA was calculated as the mean of the proximal and distal measurements obtained beyond this segment. In addition, OCT-derived flow ratio (OFR; Pulse Medical Imaging Technology, Shanghai, China) was calculated within the corresponding OCT–angiographic region of interest [15].

2.6 | Statistical Assessment

Continuous variables are reported as mean ± standard deviation (SD) or median with interquartile range (IQR), as appropriate. Categorical variables are presented as frequencies and percentages. Anatomy-physiology relationships were evaluated using quadratic regression models, with both μFR and OFR analyzed against OCT-derived %AS as a common high-resolution anatomical reference. Given the exploratory nature of this preclinical study, serial comparisons of image-derived metrics across follow-up time points were assessed using the Kruskal–Wallis test, followed by pairwise post hoc comparisons using the Mann–Whitney U test with Bonferroni correction for multiple comparisons. Where two-group comparisons were required, independent-samples t-tests were used. All statistical tests were two-sided, and a p-value < 0.05 was considered statistically significant. All analyses were performed in R version 4.3.2 (R Foundation for Statistical Computing, Vienna, Austria).

3 | Results

3.1 | Procedural Overview and Notable Events

Table 1 summarizes the angiographic, OCT-derived anatomical, and virtual physiological findings in the rabbit and mini-pig cohorts. A total of 18 RFS devices were implanted: 6 in the bilateral external iliac arteries of 3 rabbits and 12 in the bilateral profunda femoris arteries of 6 mini-pigs. All animals survived to their scheduled follow-up. Technical success of scaffold implantation was achieved in all cases except one, which is detailed in Supporting Information S1: Figure S1. In the same animal, the scheduled 1-month imaging assessment was not performed because of a carotid access-site hematoma.

In a different rabbit implant, thrombosis was identified on post-implantation intravascular OCT (Supporting Information S1: Figure S2). This was attributed by the operators to delayed heparin administration at the time of implantation. Despite the presence of substantial white thrombus, defined as platelet-rich thrombus without optical shadowing on OCT [16], 3-month follow-up demonstrated preserved anatomical patency and preserved virtual physiological indices.

3.2 | Anatomical Assessment

In rabbits, angiography demonstrated smaller vessel dimensions immediately after implantation, with RD decreasing from 2.92 mm pre-implantation to 2.08 mm post-implantation (adjusted $p < 0.01$) and MLD decreasing from 2.3 to 1.65 mm (adjusted $p = 0.05$). Between post-implantation and 3-month follow-up, reference dimensions increased, with angiographic RD rising from 2.08 to 2.54 mm (adjusted $p = 0.03$) and OCT-derived RA from 3.42 to 5.29 mm^2 (adjusted $p = 0.02$). In contrast, minimum lumen dimensions remained broadly unchanged over the same interval (angiographic MLD 1.65 vs. 1.61 mm, adjusted $p = 1.00$; OCT-derived MLA 2.60 vs. 2.27 mm^2, adjusted $p = 0.23$). Accordingly, angiographic %DS increased numerically from 20.6% to 36.2% (adjusted $p = 0.20$), whereas OCT-derived %AS increased significantly from 28.9% to 56.1% (adjusted $p < 0.01$). SL also decreased from 10.40 mm post-implantation to 8.63 mm at 3 months (adjusted $p < 0.01$).

In mini-pigs, angiographic MLD decreased from 2.95 mm pre-implantation to 2.55 mm post-implantation (adjusted $p = 0.02$), whereas RD remained similar (3.31 vs. 3.11 mm, adjusted $p = 0.96$). The dominant anatomical changes occurred between post-implantation and 1 month, with reductions in angiographic MLD (2.55–1.67 mm, adjusted $p < 0.01$) and OCT-derived MLA (6.18–2.74 mm^2, adjusted $p < 0.01$), accompanied by increases in angiographic %DS (to 48.1%, adjusted $p < 0.01$) and OCT-derived %AS (to 61.3%, adjusted $p < 0.01$). From 1 to 3 months, these parameters remained broadly stable. SL decreased from 25.68 mm post-implantation to 21.07 mm at 1 month and remained unchanged at 3 months (21.06 mm), corresponding to an overall reduction of 17.9% from post-implantation to 3 months (adjusted $p < 0.01$).

3.3 | Virtual Physiological Assessment

In rabbits, μFR decreased from 0.99 post-implantation to 0.92 at 3 months (adjusted $p = 0.04$). In contrast, OFR remained unchanged over the same interval (0.97 vs. 0.97, adjusted $p = 0.16$). In mini-pigs, μFR decreased from 0.97 post-implantation to 0.86 at 1 month (adjusted $p < 0.01$), while OFR decreased from 0.98 to 0.93 (adjusted $p = 0.03$). Between 1 and 3 months, both indices remained stable, with μFR changing from 0.86 to 0.87 and OFR from 0.93 to 0.92, without significant interval change. Figure 2 illustrates representative imaging from a mini-pig case.

Pooling post-implantation and follow-up observations from both species demonstrated inverse curvilinear relationships

TABLE 1 | Serial angiographic and OCT-derived anatomical and virtual physiological measurements after RFS implantation in rabbit and mini-pig models.

		Angiography				OCT				
Time point	***N***	**RD (mm)**	**MLD (mm)**	**%DS**	**μFR**	**RA (mm^2)**	**MLA (mm^2)**	**%AS**	**SL (mm)**	**OFR**
Rabbit model										
Pre	6	2.92 (0.41)	2.35 (0.36)	19.7 (5.0)	0.99 (0.01)	—	—	—	—	—
Post	6	2.08 (0.10)	1.65 (0.33)	20.6 (16.0)	0.99 (0.01)	3.42 (0.37)	2.60 (0.62)	28.9 (25.4)	10.40 (0.13)	0.97 (0.03)
3M	6	2.54 (0.32)	1.61 (0.21)	36.2 (6.9)	0.92 (0.05)	5.29 (1.35)	2.27 (0.53)	56.1 (9.3)	8.63 (0.28)	0.97 (0.01)
Pairwise comparisons										
Pre versus Post		< 0.01	0.05	1.00	0.59	—	—	—	—	—
Post versus 3M		0.03	1.00	0.20	0.04	0.02	0.23	< 0.01	< 0.01	0.16
Mini-pig model										
Pre	12	3.31 (0.21)	2.95 (0.24)	10.7 (5.0)	0.99 (0.01)	8.64 (1.10)	6.87 (1.09)	20.3 (8.6)	—	0.99 (0.01)
Post	12	3.11 (0.36)	2.55 (0.30)	17.8 (7.1)	0.97 (0.03)	7.97 (1.70)	6.18 (0.88)	30.9 (12.8)	25.68 (0.59)	0.98 (0.02)
1 M	10	3.20 (0.33)	1.67 (0.32)	48.1 (6.7)	0.86 (0.15)	8.02 (1.44)	2.74 (0.94)	61.3 (16.7)	21.07 (0.98)	0.93 (0.05)
3 M	10	3.48 (0.32)	1.86 (0.28)	45.8 (8.1)	0.87 (0.13)	9.52 (1.75)	3.26 (1.00)	63.2 (13.5)	21.06 (1.44)	0.92 (0.06)
Pairwise comparisons										
Pre versus Post		0.96	0.02	0.68	0.08	1.00	0.68	1.00	—	1.00
Post versus 1 M		1.00	< 0.01	< 0.01	< 0.01	1.00	< 0.01	< 0.01	< 0.01	0.03
Post versus 3 M		0.30	< 0.01	< 0.01	0.04	0.53	< 0.01	< 0.01	< 0.01	0.02
1 M versus 3 M		0.56	0.99	1.00	1.00	0.56	1.00	1.00	1.00	1.00

Note: Data are presented as mean (SD). *N* denotes the number of imaged vessels/scaffolds; each animal underwent bilateral implantation. Pairwise comparisons are shown as Bonferroni-adjusted p values for the contrasts listed. (—) indicates not available or not applicable. Pre-implantation OCT was not performed in the rabbit model. In one mini-pig, 1-month imaging was not performed owing to a carotid access-site hematoma. In another mini-pig, both angiographic and OCT data were unavailable for analysis because of electronic data loss.

Abbreviations: %AS, percent area stenosis; %DS, percent diameter stenosis; 1M, 1-month follow-up; 3M, 3-month follow-up; MLA, minimum lumen area; MLD, minimum lumen diameter; OFR, OCT-derived flow ratio; Post, post-implantation; Pre, pre-implantation; RA, reference area; RD, reference vessel diameter; SL, scaffold length; μFR, angiography-derived Murray-law-based quantitative flow ratio.

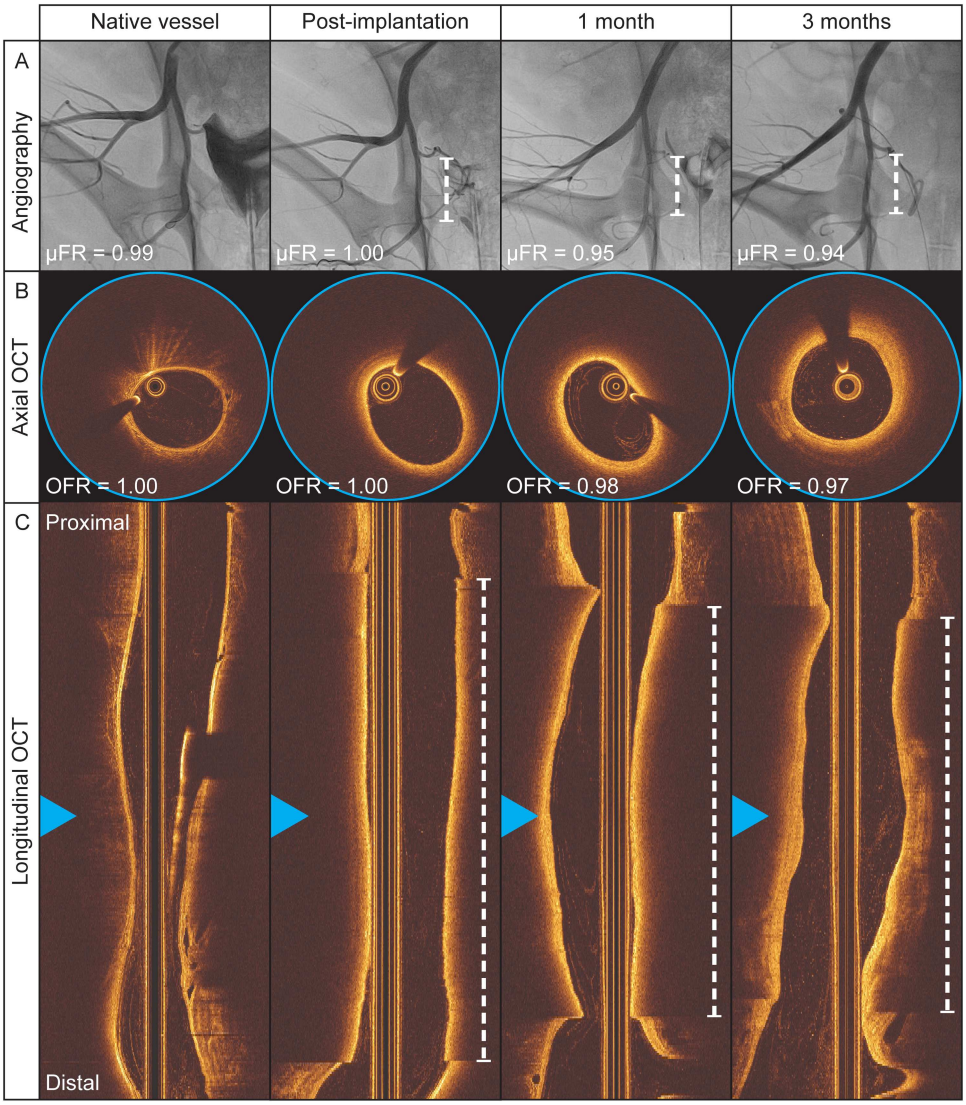

FIGURE 2 | Serial multimodality imaging and representative virtual physiology following resorbable fibrillated scaffold implantation. Representative angiography, axial OCT, and longitudinal OCT acquired from a mini-pig target vessel at baseline (native vessel), post-implantation, 1 month, and 3 months. (A) Angiography with corresponding μFR values from post-implantation onward. (B) Axial OCT with corresponding OFR values from post-implantation onward. (C) Longitudinal OCT demonstrating serial scaffold–lumen morphology. Blue arrowheads indicate the approximate location of the axial OCT frame shown in panel B, and white dashed brackets denote the scaffolded segment. [Color figure can be viewed at wileyonlinelibrary.com]

between OCT-derived %AS and both virtual physiological indices (Figure 3). μFR and OFR each declined with increasing %AS, with similar model fit for μFR-AS and OFR-AS ($R^2 = 0.57$). Follow-up observations were generally associated with higher OCT-derived %AS than post-implantation observations. Despite this, most μFR and OFR values remained above the 0.80 reference threshold, with the exception of a single outlier animal case.

4 | Discussion

This preclinical study supports the procedural feasibility of RFS implantation across both animal models. Technical success was achieved in all but one case, and the overall short-term procedural profile was favorable. Two notable exceptions merit comment. In one vessel, late imaging demonstrated a markedly abnormal double-lumen configuration with severe narrowing of the dominant channel and substantially reduced virtual physiological indices (Supporting Information S1: Figure S1), most plausibly reflecting undersizing at implantation, possibly related to transient vasospasm and underestimation of the true reference vessel diameter. In a separate rabbit case, immediate post-implantation white thrombus was visualized on OCT (Supporting Information S1: Figure S2), but this was attributed to delayed heparin administration and had resolved by 3-month follow-up, with preserved vessel patency and virtual physiological indices. Taken together, these findings suggest that although important procedural and imaging outliers occurred, they did not represent the dominant pattern of device behavior.

A consistent finding across both models was that the scaffolded segment underwent measurable geometric evolution after implantation, as demonstrated by serial angiographic and OCT

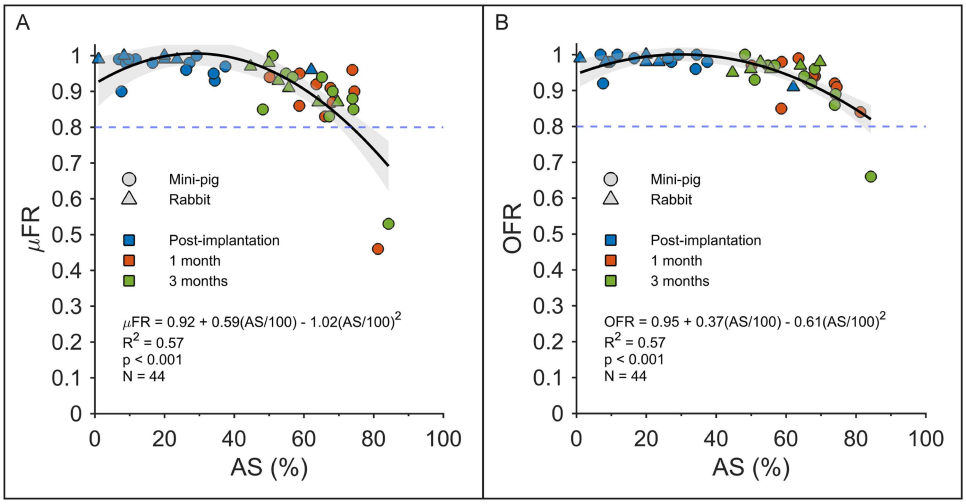

FIGURE 3 | Anatomy-physiology relationships in serial preclinical observations. Quadratic regression analysis of angiography-derived μFR and OCT-derived OFR against OCT-derived percent area stenosis (%AS) in matched serial observations from rabbit and mini-pig models ($N = 44$). (A) μFR plotted against %AS. (B) OFR plotted against %AS. Regression curves are shown in black, with 95% confidence bands in gray. The horizontal blue dashed line indicates a physiological reference value of 0.80. Marker shape denotes animal model, and marker color denotes follow-up time point. Both analyses demonstrated non-linear inverse relationships between OCT-derived anatomical stenosis severity and virtual physiological indices, with most observations remaining above the 0.80 reference value despite greater stenosis severity at follow-up. Equations are displayed with AS expressed as percentage values divided by 100. [Color figure can be viewed at wileyonlinelibrary.com]

assessments. Across both species, changes in lumen dimensions and scaffold length were most evident early after implantation and then showed relative stabilization over follow-up. These findings suggest that the scaffold does not remain geometrically static after deployment, but instead undergoes an early phase of structural adaptation followed by later stabilization.

The mechanisms underlying this evolution cannot be determined definitively from the present dataset. Plausible, non-mutually exclusive explanations may differ across phases of follow-up and by the specific geometric change observed. Early shortening may reflect structural relaxation and reconfiguration of the fibrillated polymeric microfibre network, whereas later changes in lumen geometry may be influenced by progressive tissue integration into the porous scaffold matrix [12], and healing-related vascular remodeling, including effects related to near-wall hemodynamics such as endothelial shear stress [17]. Because the OCT appearance of the scaffold also changed over time (Supporting Information S1: Figure S3), some contribution from serial image delineation of scaffold boundaries cannot be excluded. These interpretations should be regarded as hypotheses rather than proven mechanisms. Nonetheless, the consistent observation of scaffold shortening across both species suggests that shortening is a genuine feature of scaffold evolution and highlights the need for longer-term study of this dynamic scaffold-vessel relationship. This may also have practical implications for future clinical implantation strategy, including lesion-length selection and device positioning.

Despite progressive anatomical change after RFS implantation, the physiological impact remained limited. Although follow-up observations showed greater anatomical narrowing, most μFR and OFR values remained above the 0.80 reference threshold. These findings indicate that anatomical progression and physiological impairment were related, but not interchangeable. In practical terms, anatomical imaging alone may overstate the functional significance of scaffold-related lumen narrowing, whereas virtual physiological assessment provides complementary information about whether these changes are likely to result in meaningful flow limitation. Integrated anatomical and virtual physiological assessment may therefore provide a more complete understanding of device behavior over time.

In this exploratory analysis, the 0.80 cut-off shown in Figure 3 should be regarded only as a reference benchmark, not as a validated ischemic cut-off for these preclinical peripheral vessels. It was adopted from human coronary pressure-wire physiology. In the coronary circulation, fractional flow reserve was established as a lesion-specific functional index and remains widely used with a treatment threshold of ≤ 0.80 [18, 19]. Its purpose here is therefore illustrative rather than prescriptive: it provides a useful frame of reference for visualizing the extent to which increasing anatomical stenosis did, or did not, correspond to substantial reduction in virtual physiological indices.

Emerging peripheral literature supports this broader conceptual approach. Feasibility studies using intravascular ultrasound and CT angiography suggest that peripheral imaging datasets can be extended to derive lesion-specific physiological information [20, 21]. In parallel, invasive fractional flow reserve, including when combined with OCT, has also been explored in BTK-arterial disease, further supporting the plausibility of physiology-guided lesion evaluation in the peripheral circulation [22, 23]. As these approaches remain preliminary and lack universally validated thresholds, they are best viewed as supporting this general framework rather than defining a fixed intervention cut-off.

μFR and OFR showed broadly concordant behavior, although OFR values were generally slightly higher than μFR. This difference may partly reflect the distinct imaging bases of the two

approaches. OFR is derived from high-resolution OCT, which provides detailed in vivo delineation of the lumen contour and therefore a precise representation of vessel geometry [16, 24]. By contrast, μFR in the present study was derived from angiography, which has lower spatial resolution and was limited to a single anteroposterior projection [14]. As a result, the angiographic reconstruction may be more susceptible to projectional error, particularly in eccentric or non-circular lesions, or when vessel angulation causes foreshortening. This may have contributed to the greater perturbation seen in μFR. Since formal agreement testing was not performed, and this was not the aim of the present study, these findings should not be overinterpreted as evidence that one modality is definitively superior to the other. Rather, they support the broader feasibility of both OCT- and angiography-based virtual physiological assessment in scaffolded peripheral vessels.

4.1 | Limitations

This study has several limitations. First, the sample size was modest, and the study should be regarded as exploratory; no prospective sample size or power calculation was performed. Second, the experiments were performed in healthy, non-stenotic peripheral arteries rather than diseased human vessels, and therefore primarily assess scaffold behavior and biocompatibility in normal arterial tissue rather than therapeutic performance in atherosclerotic lesions. Third, both μFR and OFR were developed in the coronary circulation and have not been formally validated in peripheral arteries or in these preclinical vascular beds. However, emerging exploratory studies suggest that the underlying computational principles may be transferable to the lower-limb circulation, supporting their use here as exploratory and comparative measures rather than definitive physiological endpoints. In addition, the conventional ischemic threshold discussed is a coronary-derived reference value rather than a validated peripheral cut-off in this setting. Fourth, follow-up was limited to 3 months. While the present study provides insight into early anatomical and virtual physiological behavior, it does not define the full time course of scaffold integration, degradation, or complete bioresorption. Longer-term studies, ideally including histopathological correlation, will therefore be required.

5 | Conclusion

This preclinical study supports the feasibility of RFS implantation in peripheral arteries and demonstrates that the device undergoes early structural evolution after deployment. Virtual physiological assessment revealed that these anatomical changes were accompanied by measurable reductions in flow indices, with most values remaining above the 0.80 reference threshold throughout follow-up. Together, these findings provide a basis for further development of the technology and for future studies incorporating both anatomical and virtual physiological assessment.

Acknowledgments

This study was funded by STENTiT B.V.

Conflicts of Interest

GvB and BS hold equity interests in STENTiT B.V. RdV is an employee of STENTiT B.V., serving as a preclinical engineer, while KvN is responsible for overseeing the company's clinical activities. All other authors stated that the research was performed without any commercial or financial associations that could be perceived as constituting a conflict of interest.

Data Availability Statement

The authors have nothing to report.

References

1. M. S. Kim, J. Hwang, D. K. Yon, et al., "Global Burden of Peripheral Artery Disease and Its Risk Factors, 1990-2019: A Systematic Analysis for the Global Burden of Disease Study 2019," *Lancet Global Health* 11, no. 10 (2023): e1553–e1565.

2. M. S. Conte, A. W. Bradbury, P. Kolh, et al., "Global Vascular Guidelines on the Management of Chronic Limb-Threatening Ischemia," *European Journal of Vascular and Endovascular Surgery* 58, no. 1s (2019): S1–S109.e33.

3. P. W. Serruys, H. M. Garcia-Garcia, and Y. Onuma, "From Metallic Cages to Transient Bioresorbable Scaffolds: Change in Paradigm of Coronary Revascularization in the Upcoming Decade?," *European Heart Journal* 33, no. 1 (2012): 16–25.

4. P. K. Bowen, E. R. Shearier, S. Zhao, et al., "Biodegradable Metals for Cardiovascular Stents: From Clinical Concerns to Recent Zn-Alloys," *Advanced Healthcare Materials* 5, no. 10 (2016): 1121–1140.

5. Y. Katagiri, P. W. Serruys, T. Asano, et al., "How Does the Failure of Absorb Apply to the Other Bioresorbable Scaffolds? An Expert Review of First-in-Man and Pivotal Trials," *EuroIntervention* 15, no. 1 (2019): 116–123.

6. Y. Sato, M. Kutnya, B. Abebe, et al., "Histological Assessment of a Novel Restorative Coronary Artery Bypass Graft in a Chronic Ovine Model," *Frontiers in Bioengineering and Biotechnology* 13 (2025): 1488794.

7. C. Collet, T. Asano, Y. Miyazaki, et al., "Late Thrombotic Events After Bioresorbable Scaffold Implantation: A Systematic Review and Meta-Analysis of Randomized Clinical Trials," *European Heart Journal* 38, no. 33 (2017): 2559–2566.

8. M. Ono, S. Kageyama, N. O'Leary, et al., "1-Year Patency of Bioestorative Polymeric Coronary Artery Bypass Grafts in an Ovine Model," *JACC: Basic to Translational Science* 8, no. 1 (2023): 19–34.

9. K. Miyashita, K. Ninomiya, A. Tobe, et al., "Long-Term Outcomes Following Bioresorbable Vascular Scaffolds," *Expert Review of Cardiovascular Therapy* 22, no. 8 (2024): 391–407.

10. R. L. Varcoe, S. A. Parikh, B. G. DeRubertis, et al., "Evaluation of an Infrapopliteal Drug-Eluting Resorbable Scaffold: Design Methodology for the LIFE-BTK Randomized Controlled Trial," *Journal of the Society for Cardiovascular Angiography & Interventions* 2, no. 4 (2023): 100964.

11. R. L. Varcoe, B. G. DeRubertis, R. Kolluri, et al., "Drug-Eluting Resorbable Scaffold Versus Angioplasty for Infrapopliteal Artery Disease," *New England Journal of Medicine* 390, no. 1 (2024): 9–19.

12. R. Duijvelshoff, M. S. Cabrera, B. Sanders, et al., "Transcatheter-Delivered Expandable Bioresorbable Polymeric Graft With Stenting Capacity Induces Vascular Regeneration," *JACC: Basic to Translational Science* 5, no. 11 (2020): 1095–1110.

13. L. Hatzikostas, K. Miyashita, R. de Vries, et al., "Preclinical Serial Shear Stress Analysis of a Novel Strut-Free Fibrillated Bioresorbable Polymeric Endoluminal Graft," *Frontiers in Cardiovascular Medicine* 13 (2026): 1744904.

14. S. Tu, D. Ding, Y. Chang, C. Li, W. Wijns, and B. Xu, "Diagnostic Accuracy of Quantitative Flow Ratio for Assessment of Coronary

Stenosis Significance From a Single Angiographic View: A Novel Method Based on Bifurcation Fractal Law," *Catheterization and Cardiovascular Interventions* 97, no. Suppl 2 (2021): 1040–1047.

15. W. Yu, J. Huang, D. Jia, et al., "Diagnostic Accuracy of Intracoronary Optical Coherence Tomography-Derived Fractional Flow Reserve for Assessment of Coronary Stenosis Severity," *EuroIntervention* 15, no. 2 (2019): 189–197.

16. M. Araki, S. J. Park, H. L. Dauerman, et al., "Optical Coherence Tomography in Coronary Atherosclerosis Assessment and Intervention," *Nature Reviews Cardiology* 19, no. 10 (2022): 684–703.

17. E. K. W. Poon, X. Wu, J. Dijkstra, et al., "Angiography and Optical Coherence Tomography Derived Shear Stress: Are They Equivalent in My Opinion?," *International Journal of Cardiovascular Imaging* 39, no. 10 (2023): 1953–1961.

18. N. H. J. Pijls, B. De Bruyne, K. Peels, et al., "Measurement of Fractional Flow Reserve to Assess the Functional Severity of Coronary-Artery Stenoses," *New England Journal of Medicine* 334, no. 26 (1996): 1703–1708.

19. J. S. Lawton, J. E. Tamis-Holland, S. Bangalore, et al., "2021 ACC/AHA/SCAI Guideline for Coronary Artery Revascularization: Executive Summary," *Journal of the American College of Cardiology* 79, no. 2 (2022): 197–215.

20. T. Shimada, Y. Iwasaki, A. Funatsu, T. Kobayashi, S. Nakamura, and D. Fukuda, "Intravascular Ultrasound-Derived Virtual Fractional Flow Reserve in the Superficial Femoral Artery," *CVIR Endovascular* 7, no. 1 (2024): 92.

21. E. P. Ward, D. Shiavazzi, D. Sood, et al., "Computed Tomography Fractional Flow Reserve Can Identify Culprit Lesions in Aortoiliac Occlusive Disease Using Minimally Invasive Techniques," *Annals of Vascular Surgery* 38 (2017): 151–157.

22. Z. Ruzsa, S. Róna, G. G. Tóth, et al., "Fractional Flow Reserve in below the Knee Arteries With Critical Limb Ischemia and Validation Against Gold-Standard Morphologic, Functional Measures and Long Term Clinical Outcomes," *Cardiovascular Revascularization Medicine* 19, no. 2 (2018): 175–181.

23. C. van Wely, R. J. Oosterveld, L. H. Bouwman, I. Fourneau, A. W. J. van 't Hof 't, and O. Yazar, "Optical Coherence Tomography and Fractional Flow Reserve in Below-the-Knee Percutaneous Transluminal Angioplasty: A Pilot Study," *CVIR Endovascular* 8, no. 1 (2025): 87.

24. T. Xu, W. Yu, D. Ding, et al., "Diagnostic Performance of Intracoronary Optical Coherence Tomography-Modulated Quantitative Flow Ratio for Assessing Coronary Stenosis," *Journal of the Society for Cardiovascular Angiography & Interventions* 2, no. 5 (2023): 101043.

Supporting Information

Additional supporting information can be found online in the Supporting Information section.

Supporting File 1: ccd70752-sup-0001-STENTiT_CCI_SUPPLEMENT.docx.